

## Supplementary Material for

# Simultaneous ultraviolet, visible and near-infrared continuous-wave lasing in a rare-earth-doped microcavity

Bo Jiang,<sup>a</sup> Song Zhu,<sup>a,b</sup> Linhao Ren,<sup>a</sup> Lei Shi,<sup>a,c,\*</sup> and Xinliang Zhang<sup>a,c</sup>

<sup>a</sup>Wuhan National Laboratory for Optoelectronics, Huazhong University of Science and Technology, Wuhan 430074, China

<sup>b</sup>School of Electrical and Electronic Engineering, Nanyang Technological University, 50 Nanyang Avenue, 639798, Singapore

<sup>c</sup>Optics Valley Laboratory, Wuhan 430074, China

\*Corresponding Author, E-mail: lshi@hust.edu.cn

**Keywords:** Multi-band microlasers, Whispering-gallery microcavities, Rare earth elements, Upconversion

## 1. Fabrication of the ultrahigh-Q RE-doped microcavities

The fabrication process is as follows (Fig. S1): Firstly, the Er-Yb-PMMA solution is prepared by mixing erbium nitrate pentahydrate (99.9%, Maklin), ytterbium nitrate pentahydrate (99.99%, Maklin), PMMA (TCI), and acetone (AR, Shanghai Hushi) with a weight ratio of 1:2.5:15.82:415.79. Secondly, obtain a microbottle cavity from a standard single-mode optical fiber by CO<sub>2</sub> laser fabrication platform. Thirdly, dip the microbottle into the Er-Yb-PMMA solution and then draw it out. After evaporation, an Er-Yb-PMMA film will homogeneously form on the surface of the microbottle. Finally, the Er-Yb-PMMA microbottle is sufficiently heated to form an Er-Yb co-doped microsphere by heat reflow process. During the heat reflow process, PMMA is eliminated due to high temperature, and Er and Yb ions are melted into the microcavity without obvious ion clusters.

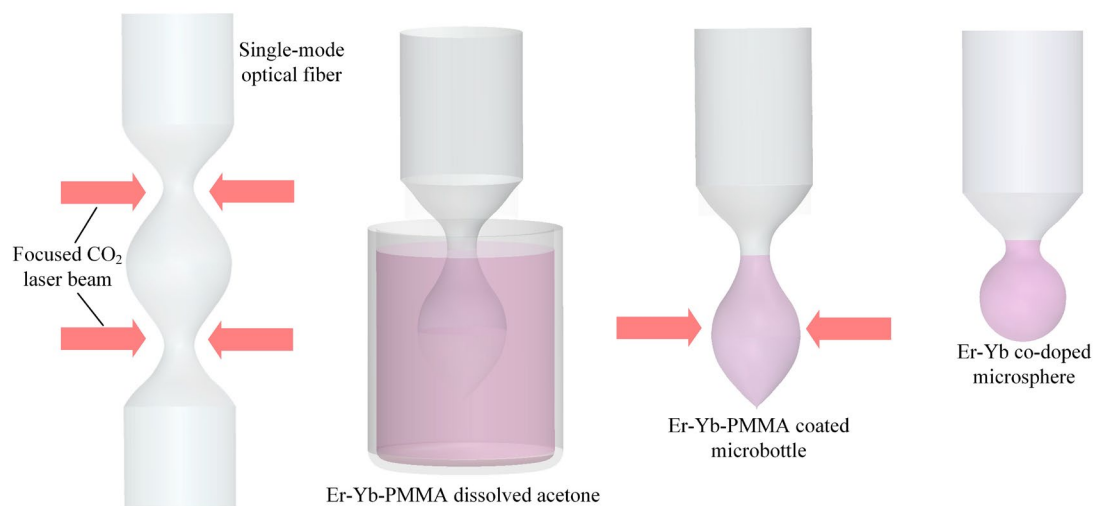


**Fig. S1.** Fabrication process of an Er-Yb co-doped microsphere cavity.

The microsphere size can be flexibly controlled by adjusting the spot sizes of the focused CO<sub>2</sub> laser beams and the relative positions between the microsphere and the laser spots. Smaller spot sizes of the focused CO<sub>2</sub> laser beams along with a larger spacing between the two CO<sub>2</sub> laser beams will obtain a larger microsphere. Ultrahigh-Q RE-doped microcavity can be efficiently fabricated by this doping method. In this fabrication process, with the assistance of PMMA, obvious RE ion clusters have been avoided well. As shown in Fig. S2, all of the PMMA-assisted RE-doped microcavities have Q factors over  $5 \times 10^7$ , including thirteen microspheres with Q factors exceeding  $10^8$ . It means that this fabrication process possesses a good reproducibility. In contrast, the RE-doped microcavities without the assistance of PMMA exhibit much lower Q factors, including thirteen microspheres with Q factors below  $10^7$ .

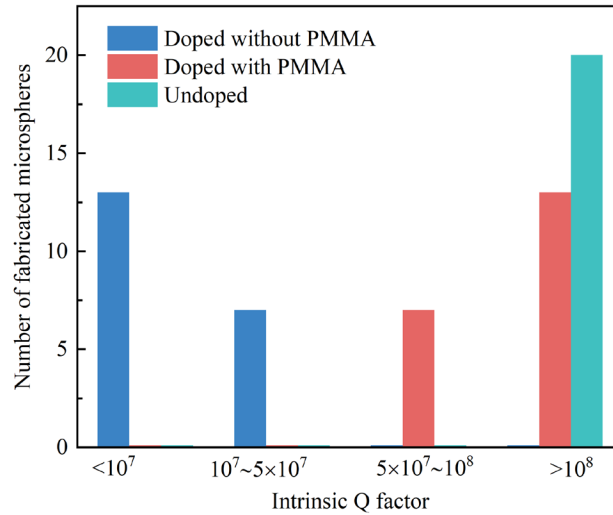


**Fig. S2.** Distribution of Q factors for sixty microspheres fabricated with different doping processes.

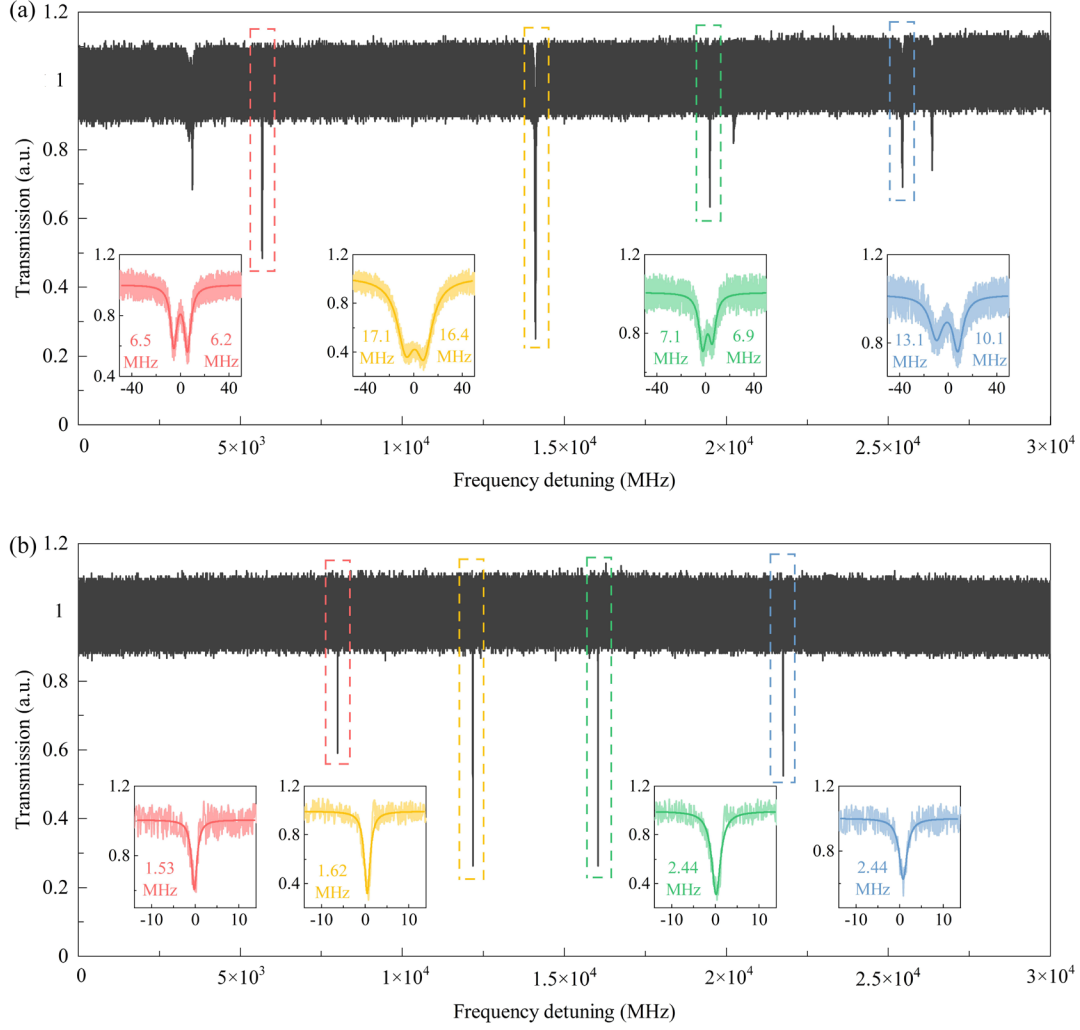


**Fig. S3.** Typical transmission spectra around 1620 nm of the Er-Yb co-doped microspheres (a) without and (b) with the assistance of PMMA. Insets: Zoom-in transmission spectra, where the fitted linewidths corresponding to the four resonance modes are exhibited.

Ion clusters acting as scatterers will induce backward scattering light in the doped microcavities. Meanwhile, the backscattering light will couple with the forward propagation light, which makes a resonance mode split into two resonance modes. Mode splitting has been used to detect single viruses and nanoparticles based on lasing in Er-doped microcavities, where a 15-nm-radius nanoparticle located at the cavity surface can induce mode splitting from 0.16 to 0.44 MHz.<sup>49</sup> Therefore, ion clusters can also be estimated by the magnitude of mode splitting. Fig. S3 shows transmission spectra over 30 GHz (close to the maximum finely sweeping span of our tunable laser), where multiple resonance modes are covered. The doped microcavity

without the assistance of PMMA exhibits mode splitting in all the resonance modes. We enlarge the transmission spectra of the four resonance modes with large extinction ratios. They possess large mode splitting up to 10.1, 13.8, 7.8, 17.1 MHz, respectively. In contrast, the PMMA-assisted doped microcavity does not show obvious mode splitting. It indicates that the PMMA-assisted doping process will not introduce obvious ion clusters. It is worth noting that, the doping process without PMMA will result in a lower doping concentration. Therefore, the RE concentration in the RE-acetone solution need to increase fivefold for achieving a similar doping concentration to the PMMA-employed doping process.

In general, this PMMA-assisted doping method is simple, low-cost and high-performance. Besides, our method can also be applied in on-chip microtoroids, in which, we can coat an Er-Yb-PMMA film on a microdisk, and then reflow it to form a microtoroid. Despite many advantages of our method, the accurate concentration and the distribution of RE ions are difficult to be measured due to the poor electrical conductivity of the cavity. The doping process relies on the diffusion of RE ions from the surface to the interior of the cavity. Considering that the cavity has a large diameter and the diffusion process is determined by the temperature and the diffusion time. The expected RE distribution is shown in Fig. S4. It can be concluded that the doping concentration around the cavity surface should be larger than that in the interior of the cavity.

The effective doping concentration is estimated in the 1550 nm-band as shown in Fig. 1(b), which takes the overlap integral between the distribution of Er ions and the mode field into account. Upconversion laser in the shorter wavelength will distribute more energy around the cavity surface, compared with downshifting laser. As a result, this will lead to an underestimate of the effective doping concentration for upconversion laser.

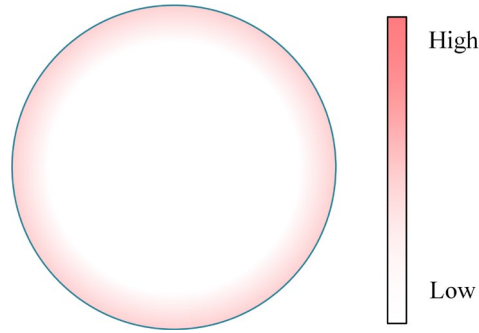
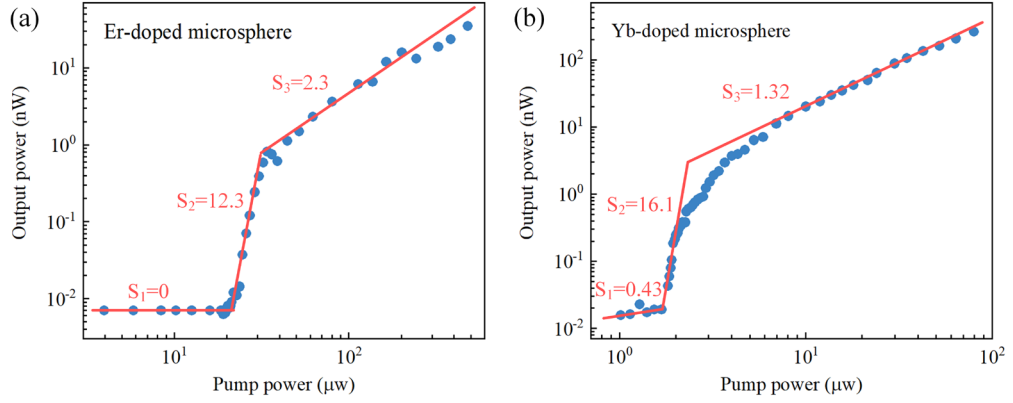


Fig. S4. Expected distribution of rare earth elements in a doped microsphere.

## 2. Competition among the lasing bands

The slopes of pump-output curves in multi-band laser are different from that in single-band laser due to the intensive competition for limited excited populations. We have measured downshifting laser in an Er-doped microsphere and an Yb-doped microsphere, as shown in Fig. S5. As they are separately doped into the microsphere, the upconversion efficiency is lowered. The lasing slopes (corresponding to phase  $S_2$ ) for the Er- and Yb-doped microspheres are estimated to be 12.3 and 16.1, respectively, which are far larger than those in the Er-Yb co-doped microsphere (as shown in Fig. 3(d), 4.43 and 2.65, respectively). Furthermore, their lasing thresholds are also reduced from 38 to 22  $\mu\text{W}$  and 10 to 2  $\mu\text{W}$ , respectively. It indicates that there is an effective energy transfer from Yb to Er, which improves the upconversion efficiency in Er and also decreases the lasing slopes of downshifting laser.



**Fig. S5.** Emission intensities in the (a) 1550 and (b) 1080 nm-bands versus the pump power in log-log scale, where  $S$  represents the slope.

We construct a simple model to describe the competition among different lasing bands, as shown in Fig. S6(a). The total loss ( $\kappa_1$ ) including the intrinsic loss and the coupling loss for a resonance mode at the downshifting wavelength is adjusted to be 1 MHz to turn on low-threshold downshifting lasing, and 100 MHz to shut down downshifting lasing. As shown in Figs. S6(b-c), the onset of downshifting lasing will result in higher thresholds and lower slopes of the pump-output curves for upconversion lasing.

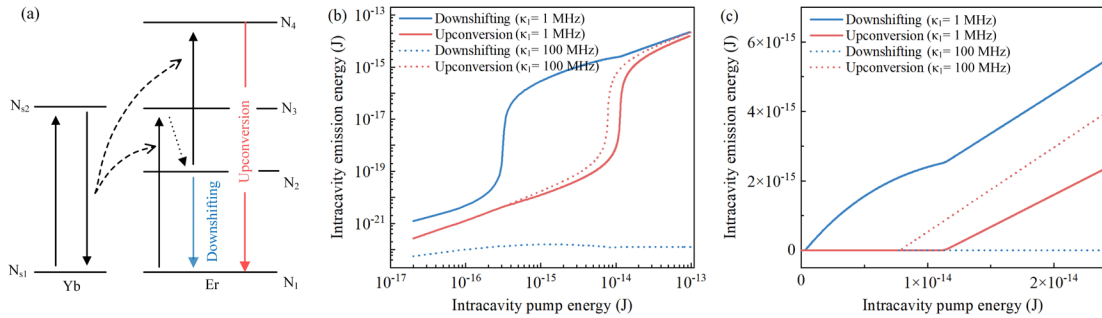


**Fig. S6.** (a) Proposed energy level diagram. Calculated intracavity emission energy versus the intracavity pump power in an Er-Yb co-doped microsphere in (b) log-log and (c) linear scales.

The rate equations used for the above mentioned calculations can be expressed as:

$$\frac{dN_1}{dt} = \frac{N_4}{t_4} + \frac{N_2}{t_2} - B_p \sigma_{p1} N_1 S_p - u N_1 N_{s2} + B_{s1} (\sigma_{s1\_em} N_2 - \sigma_{s1\_ab} N_1) S_1 + B_{s2} (\sigma_{s2\_em} N_4 - \sigma_{s2\_ab} N_1) S_2 \quad (1)$$

$$\frac{dN_2}{dt} = \frac{N_3}{t_3} - \frac{N_2}{t_2} - B_p \sigma_{p2} N_2 S_p - u N_2 N_{s2} - B_{s1} (\sigma_{s1\_em} N_2 - \sigma_{s1\_ab} N_1) S_1 \quad (2)$$

$$\frac{dN_3}{dt} = -\frac{N_3}{t_3} + B_p \sigma_{p1} N_1 S_p + u N_1 N_{s2} \quad (3)$$

$$\frac{dN_{s1}}{dt} = \frac{N_{s2}}{t_{s2}} + B_p (\sigma_{yb\_em} N_{s2} - \sigma_{yb\_ab} N_{s1}) S_p + u N_{s2} (N_1 + N_2) \quad (4)$$

$$\frac{dS_1}{dt} = \left[ \frac{c}{n} (\sigma_{s1\_em} N_2 - \sigma_{s1\_ab} N_1) - \kappa_1 \right] S_1 + \frac{\beta N_2}{t_2 B_1} \quad (5)$$

$$\frac{dS_2}{dt} = \left[ \frac{c}{n} (\sigma_{s2\_em} N_4 - \sigma_{s2\_ab} N_1) - \kappa_2 \right] S_2 + \frac{\beta N_4}{t_4 B_2} \quad (6)$$

$$0 = \frac{dN_1}{dt} + \frac{dN_2}{dt} + \frac{dN_3}{dt} \quad (7)$$

$$0 = \frac{dN_{s1}}{dt} + \frac{dN_{s2}}{dt} \quad (8)$$

Variables or parameters used in the above equations can be referred to Table S1 in the Supplementary Materials.

### 3. Theoretical analysis of the lasing spectra acquisitions

As shown in Fig. 4(d), the emission intensities of the 380 and 410 nm-bands are relatively weak. The main reasons are attributed to their relatively weak intrinsic intensities, low grating diffraction efficiencies of the spectrometer, and weak coupling coefficients between the microsphere and the optical microfiber.<sup>50</sup> The coupling coefficient between the microfiber and the microsphere is given by:<sup>51</sup>

$$k_{sf} = k_{fs}^* = \frac{\omega \mathcal{E}_0}{4} (n^2 - n_0^2) \times \iiint_V \vec{E}_f \vec{E}_s^* \exp(i\Delta\beta z) dx dy dz$$

where  $k_{sf}$  ( $k_{fs}$ ) is the coupling coefficient of a microfiber (microsphere) coupled to a microsphere (microfiber),  $V$  represents the mode volume of the microsphere,  $n$  and  $n_0$  represent the refractive indexes of silica and air,  $\vec{E}_f$  and  $\vec{E}_s$  represent the normalized mode fields of the microfiber and the microsphere, which are calculated

by  $\frac{1}{2} \iint \sqrt{\varepsilon / \mu_0} |\vec{E}_{f(s)}|^2 dx dy = 1$ , and  $\Delta\beta = \beta_f - \beta_s$  is the difference between the propagation constants of the two coupled modes. A larger coupling coefficient between the microfiber and the microcavity requires two factors. One is a large overlap between their evanescent fields, and the other is the matched propagation constant. However, it is difficult to perfectly match the propagation constants for each emission band. And also, the evanescent fractions of the WGMs for each emission band vary a lot. Generally, the longer the wavelength is, the larger evanescent fraction is.

The transmission spectrum is calculated by the FDTD method, as shown in Fig. S7. This simulation model is performed that the microfiber is located at the equator of the microsphere, and a TE-mode laser source is selected as the pump light. It can be seen that the transmission decreases as the laser wavelength gets longer.

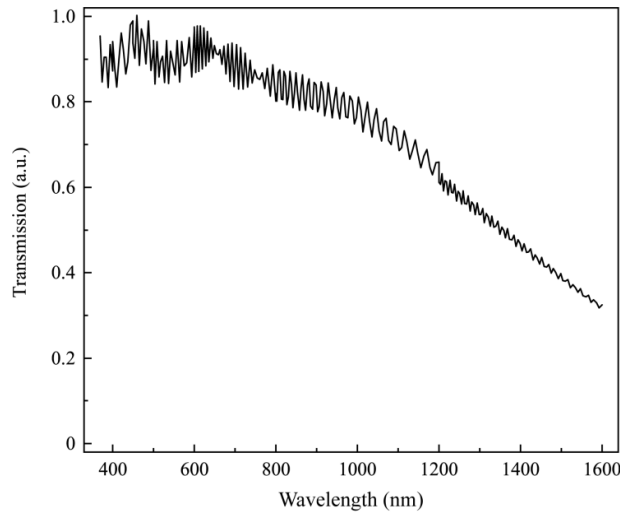


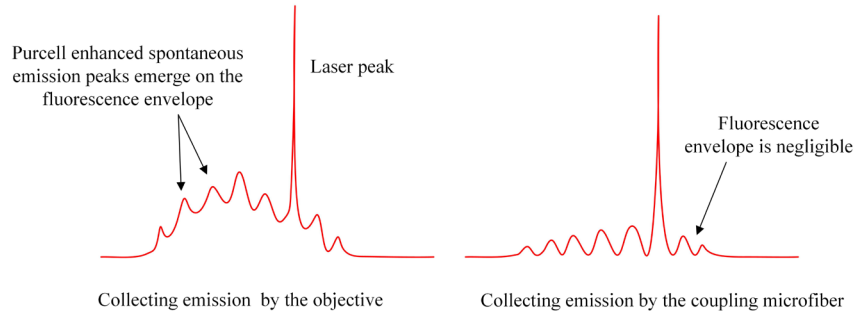
**Fig. S7.** Theoretical simulation of the transmission spectrum. The diameters of the microfiber and the microsphere are 1.2 and 57  $\mu\text{m}$ , respectively. The microfiber is glued to the equator of the microsphere.

#### 4. Detailed evolutions of the lasing spectra

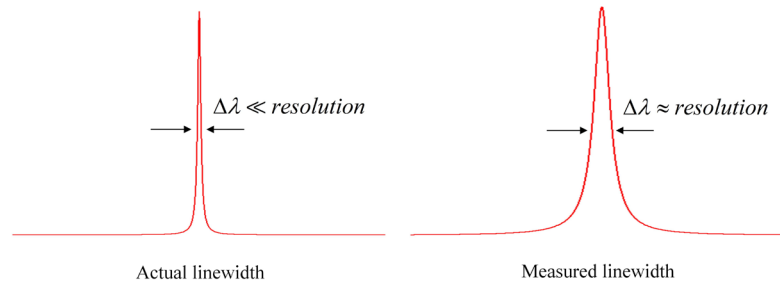
Optical spectrum acquisition is determined by the method of collecting emission and the resolution of the spectrometer, as shown in Fig. S8. As a microfiber is employed to drop the emission from the microcavity, the fluorescence envelope is negligible, while many Purcell enhanced spontaneous emission peaks emerge.<sup>32,34</sup> Limited by the resolution of the spectrometer (0.06 and 0.03 nm for upconversion and downshifting laser measurements, respectively), measured optical spectra are distorted. For nonresonant pump, the tapered fiber was coupled with WGMs with different coupling strengths. At the low pump power, there are many tiny Purcell enhanced spontaneous peaks around the major Purcell enhanced spontaneous emission peaks. These spontaneous emission peaks can be distinguished from the spectrometer introduced noise, as these spontaneous emission peaks are distributed with a spacing of one FSR. As the pump power increased, a sharp laser peak occurs while the spontaneous emission peaks annihilate gradually. This phenomenon can be attributed to the competition among these WGMs, i.e., only certain WGMs can achieve lasing. When the lasing is achieved, the lasing modes will take an advantage in competition, and other spontaneous emission peaks will be restrained.<sup>30,52</sup> As a result, from the point of view of the optical spectra, these tiny peaks fade away, exhibiting some clean laser peaks eventually. This phenomenon can be used to confirm the onset of the lasing. Fig. S9 and Fig. S10 show the lasing spectrum evolutions of the Er ion downshifting and upconversion laser, respectively. The microcavity has wider spacings between resonance modes at the longer wavelengths, and the resolution of the spectrometer for

downshifting laser is higher than that of upconversion laser, therefore, downshifting laser spectra have slighter distortion.

**Difference between the two emission collection methods**



**Distortion caused by the spectrometer resolution**



**For our measurements**

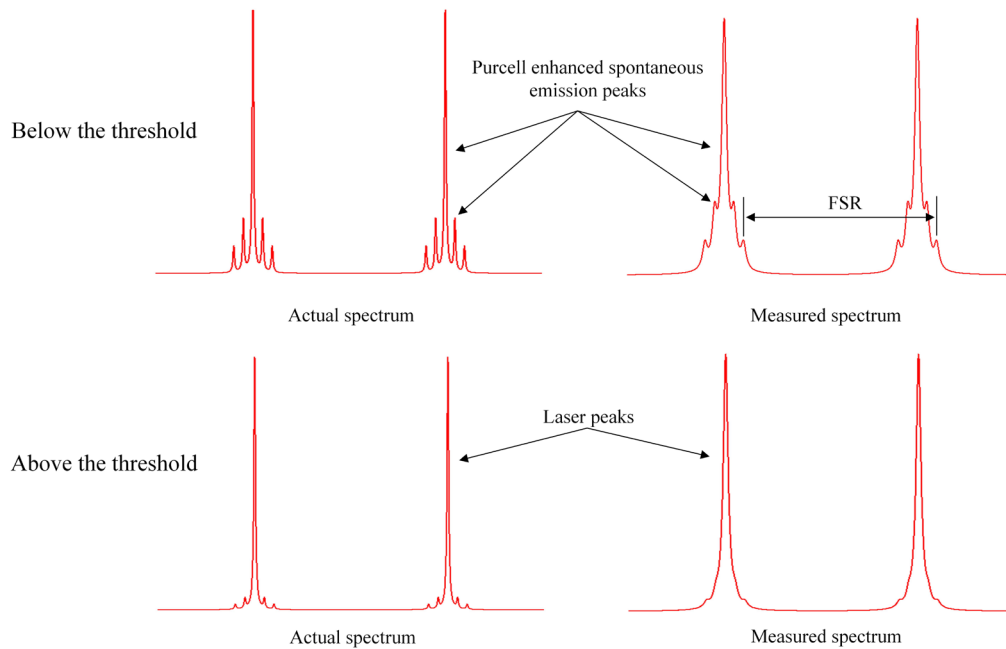


**Fig. S8.** Schematic of optical spectrum acquisition.

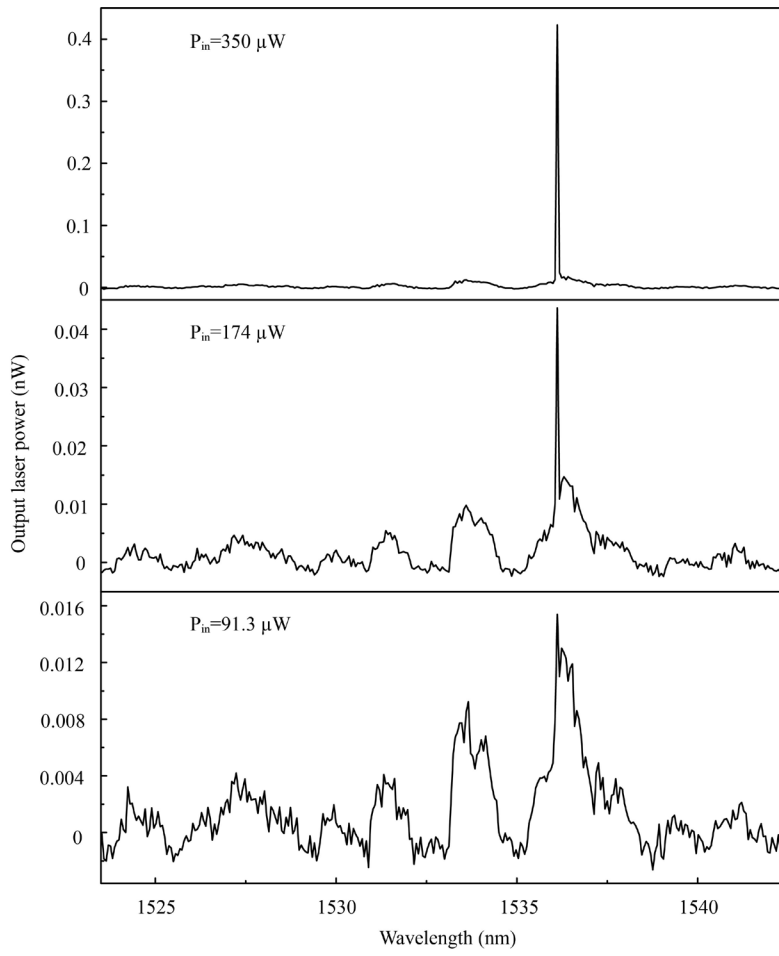


**Fig. S9.** Detailed evolution of the Er-ion downshifting spectra as the pump power increases.

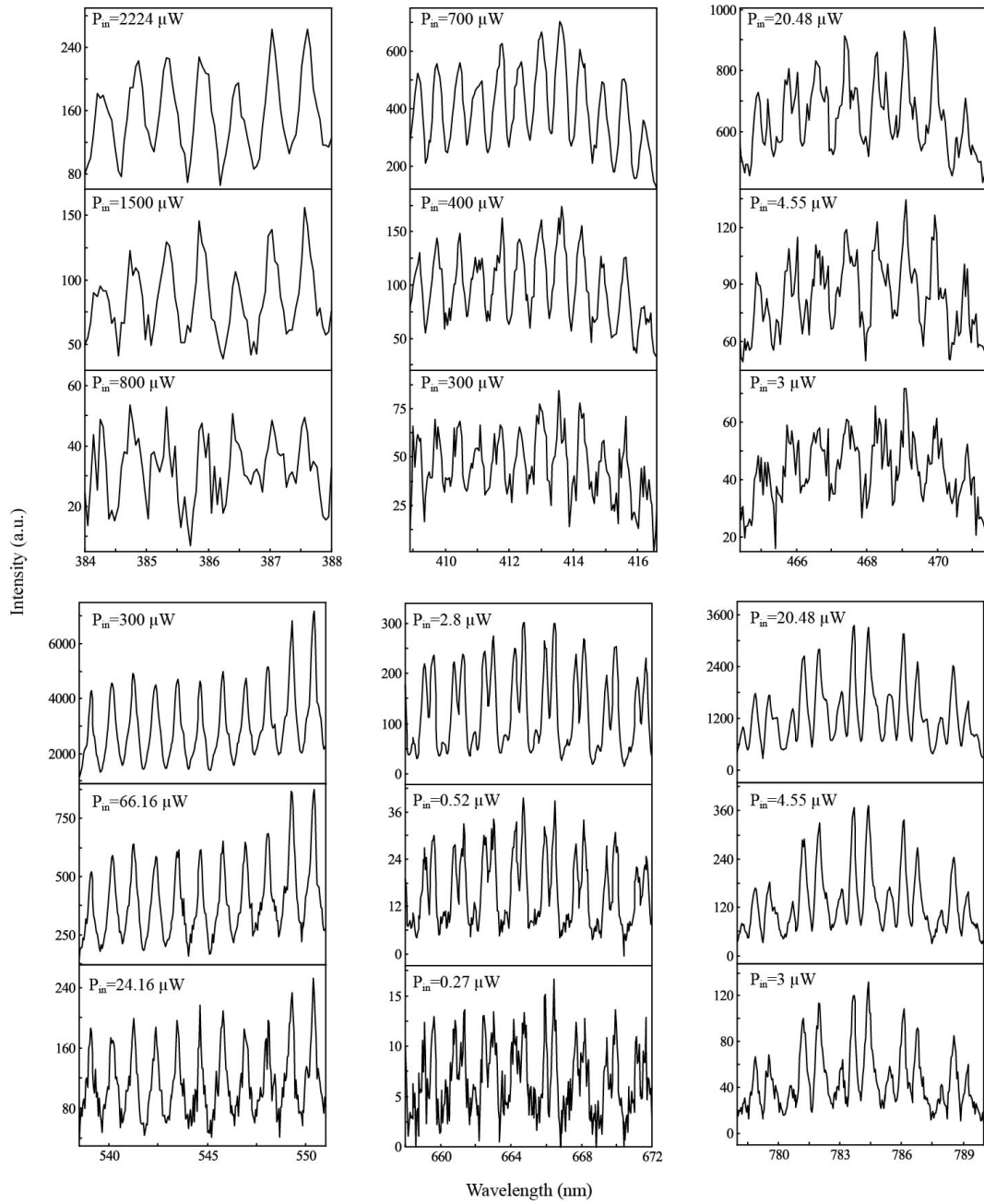


**Fig. S10.** Detailed evolutions of the Er-ion upconversion spectra as the pump power increases.

## 5. Further experimental results

Another two Er-Yb co-doped microspheres (MS1 and MS2) are also investigated.

The diameters of MS1 and MS2 are 56 and 54  $\mu\text{m}$ , respectively. They are fabricated

by using the Er-Yb-PMMA dissolved acetone with different proportions. The solution

preparations for MS1 and MS2 fabrication are mixed with the weight ratios of 1:2.5:15.82:415.79 and 1:2.67:10.55:272.19, respectively. Fig. S11 and Fig. S12 show the lasing thresholds and the spectral evolution of MS1, respectively. The thresholds of the 380, 410, 450, 560, 660, 800, 1080 and 1550 nm-bands are estimated to be 520, 180, 13, 70, 0.18, 2, 10 and 14  $\mu\text{W}$ , respectively. Fig. S13 and Fig. S14 show the thresholds and the spectral evolution of MS2, respectively. The thresholds of the 380, 410, 450, 560, 800, 1080 and 1550 nm-bands are estimated to be 700, 900, 22, 17, 10, 18, 25 and 14  $\mu\text{W}$ , respectively. The upconversion thresholds of MS2 are higher than those of MS1, due to its higher doping concentration. This is because that their absorption losses are dominated in upconversion emission bands, requiring the higher pump power to invert the energy level populations. However, with higher doping concentration in MS2, the emission intensities of the 380 and 410 nm-bands increase extremely, compared with MS1. Thus, there should be a tradeoff between the thresholds and the emission intensities of the upconversion emission bands.

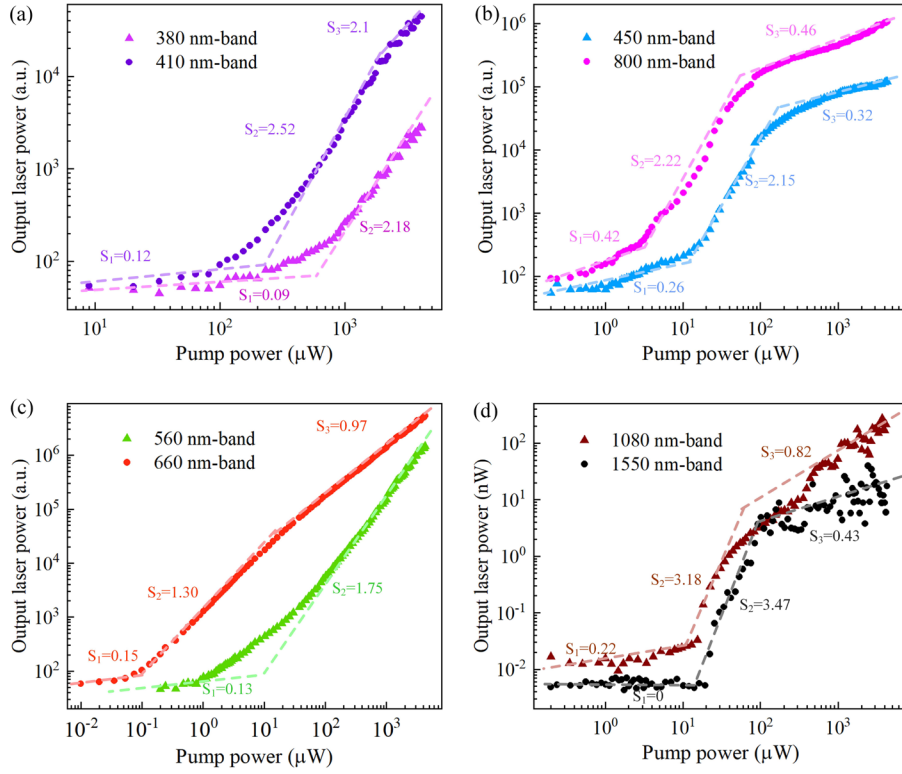


**Fig. S11.** Emission intensity of MS1 versus the pump power in log-log scale. The upconversion emission intensities are integrated from (a) 380 to 396 and 402 to 426 nm, (b) 450 to 489 and 756 to 816 nm, (c) 555 to 575 and 645 to 590 nm. (d) The downshifting emission intensities are summarized from the intensities of individual lasing wavelengths.

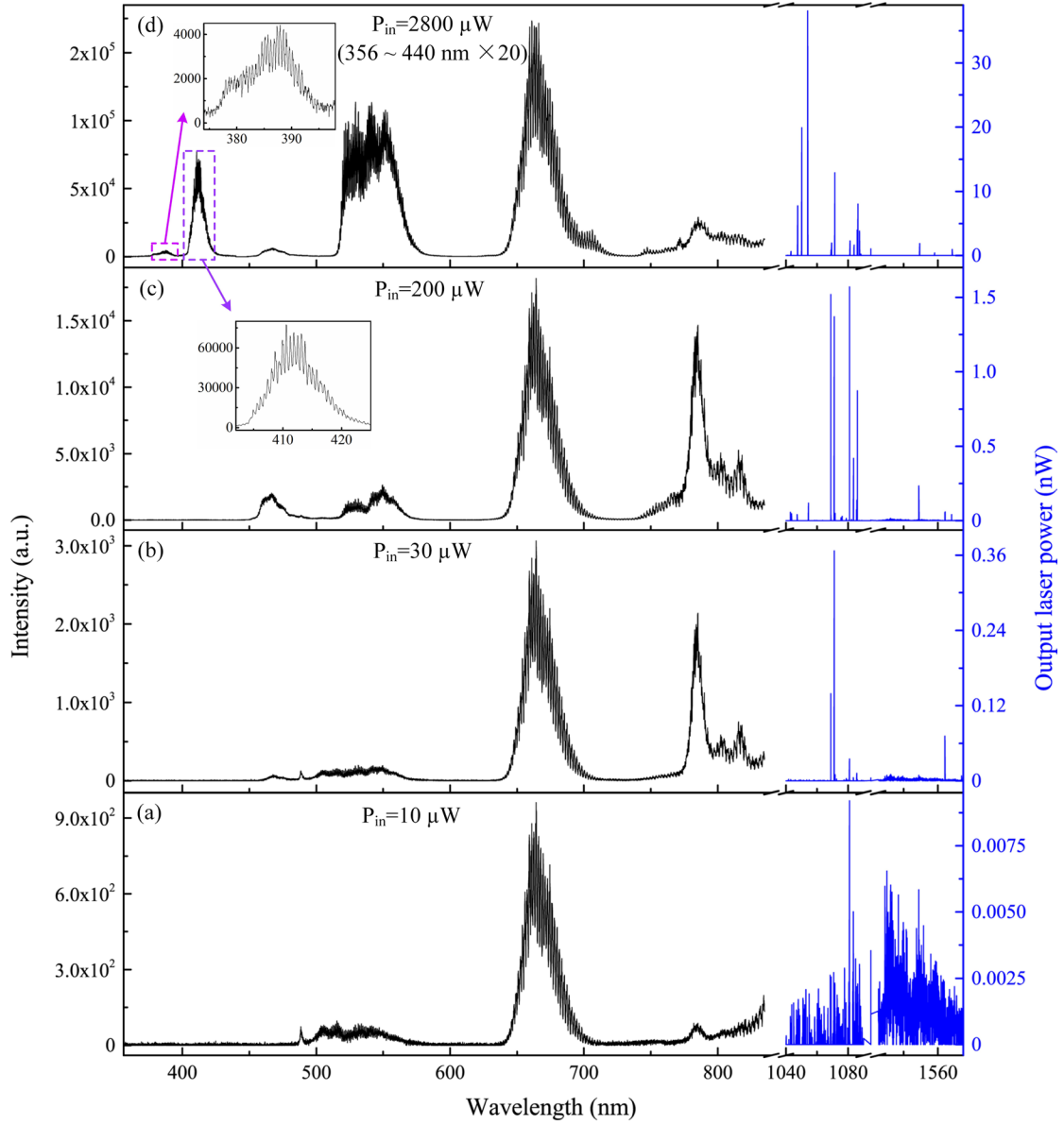


**Fig. S12.** Lasing spectrum evolution of MS1 with the increased pump power. The pump powers are (a) 10, (b) 30, (c) 200, (d) 2800  $\mu\text{W}$ , respectively, from the bottom to the top.

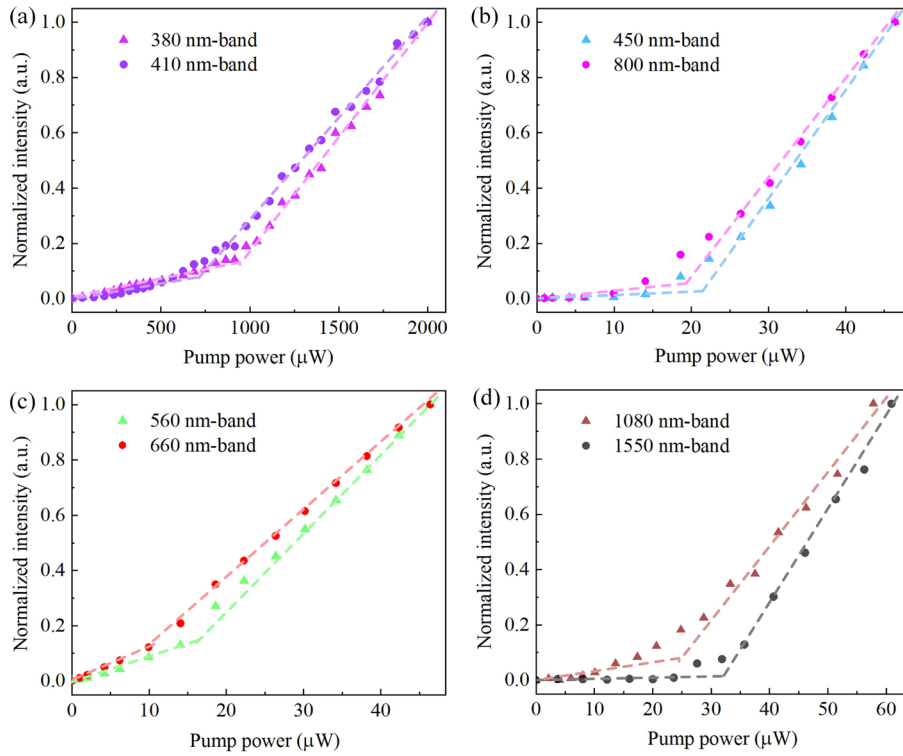


**Fig. S13.** Emission intensity of MS2 versus the pump power. The upconversion emission intensities are integrated from (a) 380 to 396 and 402 to 426 nm, (b) 450 to 489 and 756 to 816 nm, (c) 555 to 575 and 645 to 590 nm. (d) The downshifting emission intensities are summarized from the intensities of individual lasing wavelengths.

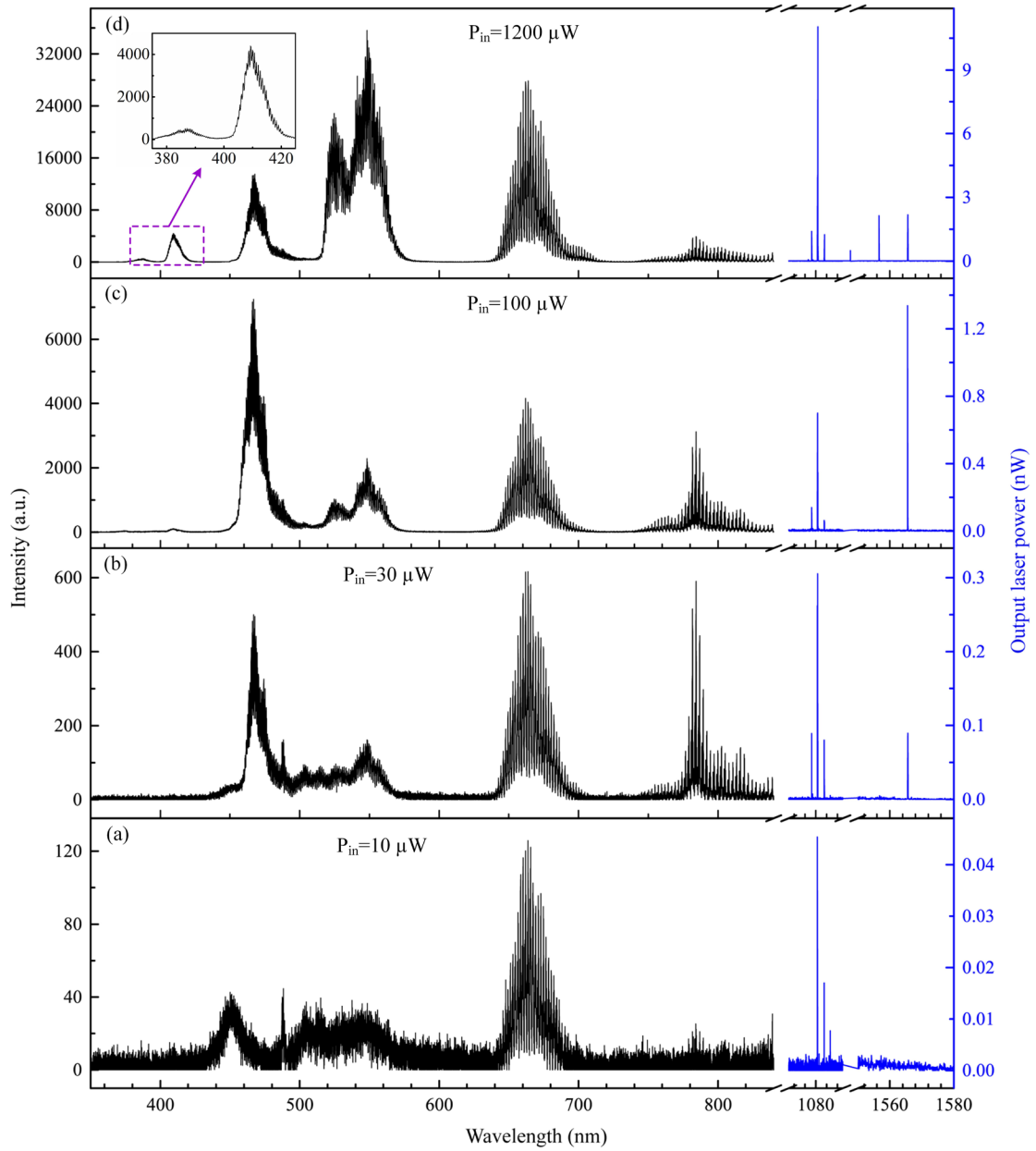


**Fig. S14.** Lasing spectrum evolution of MS2 with the increased pump power. The pump powers are (a) 10, (b) 30, (c) 100, (d) 1200  $\mu W$ , respectively, from the bottom to the top.

**Table S1.** Variables or parameters used for the rate equation calculations.

Variable or Parameter	Description	Value
$c$	Light velocity	$3 \times 10^8 \text{ m/s}$
$n$	Effective refractive index	1.35
$V$	Mode volume	$330 \mu\text{m}^3$
$h$	Planck's constant	$6.62606957 \times 10^{-34} \text{ J}\cdot\text{s}$
$\lambda_p$	Pump wavelength	980 nm
$\lambda_{s1}$	Downshifting lasing wavelength	1550 nm
$\lambda_{s2}$	Upconversion lasing wavelength	660 nm
$B$	Conversion coefficient between intracavity energy and photon flux	$\lambda/(hVn)$
$S_1$	Intracavity lasing energy of downshifting laser	
$S_2$	Intracavity lasing energy of upconversion laser	
$S_p$	Intracavity pumping energy	
$\kappa_1$	Total loss for downshifting laser	
$\kappa_2$	Total loss for upconversion laser	
$\beta$	Spontaneous radiation coupling factor	0.0001
$N_{\text{Er}}$	Concentration of Er	$1.27 \times 10^{23} / \text{m}^3$
$N_{\text{Yb}}$	Concentration of Yb	$3.18 \times 10^{23} / \text{m}^3$
$t_2$	Lifetime of $N_2$ energy level	10 $\mu\text{s}$
$t_3$	Lifetime of $N_3$ energy level	10 ms
$t_4$	Lifetime of $N_4$ energy level	250 $\mu\text{s}$
$t_{s2}$	Lifetime of $N_{s2}$ energy level	10 ms
$u$	Upconversion coefficient between Yb and Tm	$2 \times 10^{-22} \text{ m}^3/\text{s}$
$\sigma_{p1}$	Ground state absorption cross-section at pump wavelength	$2.3 \times 10^{-25} \text{ m}^2$
$\sigma_{p2}$	Excited state absorption cross-section at pump wavelength	$1 \times 10^{-25} \text{ m}^2$
$\sigma_{s1\_ab}$	Absorption cross-section for downshifting laser	$5.25 \times 10^{-25} \text{ m}^2$
$\sigma_{s1\_em}$	Emission cross-section for downshifting laser	$6 \times 10^{-25} \text{ m}^2$
$\sigma_{s2\_ab}$	Absorption cross-section for upconversion laser	$12.5 \times 10^{-25} \text{ m}^2$
$\sigma_{s2\_em}$	Emission cross-section for upconversion laser	$20 \times 10^{-25} \text{ m}^2$
$\sigma_{\text{Yb\_ab}}$	Absorption cross-section for Yb	$16 \times 10^{-25} \text{ m}^2$
$\sigma_{\text{Yb\_em}}$	Emission cross-section for Yb	$11 \times 10^{-25} \text{ m}^2$

**Table S2.** Summary of current rare-earth-based upconversion lasers.

Year	Cavity material and structure	Pump parameter	Lasing peak wavelength (nm)	Lasing threshold
2000	Er-doped ZBLAN microsphere <sup>41</sup>	800 nm, CW	527	30 $\mu$ W
2009	Er-doped silica microtoroid <sup>34</sup>	1550 nm, CW	550	690 $\mu$ W
2013	Tm-Yb co-doped silica microtoroid <sup>32</sup>	1064 nm, CW	450	17 $\mu$ W
2013	NaYF <sub>4</sub> :Yb/Er@NaYF <sub>4</sub> nanocrystal-doped silica resin microbottle <sup>36</sup>	980 nm, 6 ns, 10 Hz	410	8.5 kW/cm <sup>2</sup>
			540	4 kW/cm <sup>2</sup>
			655	5.5 kW/cm <sup>2</sup>
2016	NaYF <sub>4</sub> @NaYbF <sub>4</sub> :Tm/Gd @NaYF <sub>4</sub> nanoparticle-doped silica resin microbottle <sup>53</sup>	980 nm, 6 ns, 10 Hz	310	86 mJ/cm <sup>2</sup>
2017	NaYbF <sub>4</sub> :Gd/Tm@NaGdF <sub>4</sub> nanoparticles (random lasing) <sup>54</sup>	980 nm, 6 ns, 10 Hz	309	180 kW/cm <sup>2</sup>
2017	Yb <sup>3+</sup> -Er <sup>3+</sup> -Tm <sup>3+</sup> tridoped hexagonal $\beta$ -NaYF <sub>4</sub> microrod <sup>55</sup>	980 nm, 6 ns, 10 Hz	450	4.8 mJ/cm <sup>2</sup>
2018	NaYF <sub>4</sub> :Gd/Tm@NaGdF <sub>4</sub> nanoparticle-coated polystyrene microsphere <sup>56</sup>	1064 nm, CW	800	17 kW/cm <sup>2</sup>
			450	44 kW/cm <sup>2</sup>
2019	Er-upconverting-nanoparticle-coated plasmon cavity <sup>35</sup>	980 nm, CW	660	70 W/cm <sup>2</sup>
2020	NaYF <sub>4</sub> :Tm <sup>3+</sup> nanoparticle-coated polystyrene microsphere <sup>57</sup>	1064 nm, CW	800	1.7 $\pm$ 0.7 kW/cm <sup>2</sup>
2020	NaYF <sub>4</sub> :Yb <sup>3+</sup> , Tm <sup>3+</sup> nanoparticle-coated polystyrene microsphere <sup>58</sup>	980 nm, CW	800	14 kW/cm <sup>2</sup>
2022	NaYF <sub>4</sub> :Yb/Tm@NaErF <sub>4</sub> :Ce@NaYF <sub>4</sub> nanoparticle-doped silica toroid <sup>59</sup>	1550 nm, 6 ns, 10 Hz	290	4.8 mJ/cm <sup>2</sup>
This work	Er-Yb co-doped silica microsphere	980 nm, CW	380	480 $\mu$ W
			410	170 $\mu$ W
			450	2.7 $\mu$ W
			560	18 $\mu$ W
			660	0.18 $\mu$ W
			800	1.7 $\mu$ W
			1550	38 $\mu$ W